

Use of Power Transform Mixing Ratios as Hydrometeor Control Variables for Direct Assimilation of Radar Reflectivity in GSI En3DVar and Tests with Five Convective Storm Cases

LIANGLYU CHEN,^{a,b} CHENGSI LIU,^b MING XUE,^{b,c} GANG ZHAO,^{b,d} RONG KONG,^b AND YOUNGSUN JUNG^{b,e}

^a *Chongqing Institute of Meteorological Sciences, Chongqing, China*

^b *Center for Analysis and Prediction of Storms, University of Oklahoma, Norman, Oklahoma*

^c *School of Meteorology, University of Oklahoma, Norman, Oklahoma*

(Manuscript received 14 May 2020, in final form 8 December 2020)

ABSTRACT: When directly assimilating radar data within a variational framework using hydrometeor mixing ratios (q) as control variables (CV q), the gradient of the cost function becomes extremely large when background mixing ratio is close to zero. This significantly slows down minimization convergence and makes the assimilation of radial velocity and other observations ineffective because of the dominance of the reflectivity observation term in the cost function gradient. Using logarithmic hydrometeor mixing ratios as control variables (CV log q) can alleviate the problem but the high nonlinearity of logarithmic transformation can introduce spurious analysis increments into mixing ratios. In this study, power transform of hydrometeors is proposed to form new control variables (CV pq) where the nonlinearity of transformation can be adjusted by a tuning exponent or power parameter p . The performance of assimilating radar data using CV pq is compared with those using CV q and CV log q for the analyses and forecasts of five convective storm cases from the spring of 2017. Results show that CV pq with $p = 0.4$ (CV $pq0.4$) gives the best reflectivity forecasts in terms of root-mean-square error and equitable threat score. Furthermore, CV $pq0.4$ has faster convergence of cost function minimization than CV q and produces less spurious analysis increment than CV log q . Compared to CV q and CV log q , CV $pq0.4$ has better skills of 0–3-h composite reflectivity forecasts, and the updraft helicity tracks for the 16 May 2017 Texas and Oklahoma tornado outbreak case are more consistent with observations when using CV $pq0.4$.

KEYWORD: Data assimilation

1. Introduction

In recent years, radar reflectivity (Z) and radial velocity observations with high temporal and spatial resolution are commonly assimilated to provide more accurate initial conditions for convective-scale numerical weather prediction (NWP). Numerous studies have shown that radar data assimilation (DA) can benefit convective-scale storm analysis and forecast (e.g., Sun and Crook 1997; Xue et al. 2003; Tong and Xue 2005; Hu et al. 2006; Snook et al. 2012; Carley 2012; Yussouf et al. 2013; Johnson et al. 2015; Benjamin et al. 2016; Wang and Wang 2017). However, it is still challenging to directly assimilate radar reflectivity data within a variational framework due to the high nonlinearity of Z observation operator.

Various radar reflectivity data assimilation methods can fall into two categories: indirect or direct method; each method has its own advantages and disadvantages. Complex cloud analysis method is one of the indirect Z DA methods, which adjusts background temperature, moisture, and hydrometeor variables using radar reflectivity, satellite and surface cloud observations (Albers et al. 1996; Hu et al. 2006). Cloud analysis is

inexpensive computationally and is adopted in certain regional operational NWP systems such as the Rapid Refresh system (Benjamin et al. 2016). Studies have demonstrated positive impacts of cloud analysis for assimilating radar reflectivity data (e.g., Xue et al. 2003; Hu et al. 2006; Schenkman et al. 2011; Benjamin et al. 2016; Duda et al. 2019). However, this method relies on empirical relations to make state variable adjustments based on reflectivity observations and is not effective in suppressing spurious convection. When used in cycled data assimilation, it often overpredicts precipitation (Schenkman et al. 2011; Pan et al. 2020).

Within variational framework, Z data are sometimes indirectly assimilated through retrievals (Sun and Crook 1997). Wang et al. (2013a,b) assimilated rainwater and pseudo-water vapor data derived from radar reflectivity within WRF three-dimension variational (3DVar) and four-dimensional variational (4DVar) DA systems. Because of the prior retrieval, problems associated with the nonlinear Z operator were avoided. However, to retrieve rainwater from reflectivity which can be a function of additional hydrometeor species, warm-rain assumption was made so that ice hydrometeors were assumed to be absent. Furthermore, to avoid potentially large rainwater retrieval error based on the nonlinear reflectivity operator, only radar reflectivity < 55 dBZ were used in their studies.

To directly assimilate Z , the ensemble Kalman filter (EnKF; Evensen 1994) is an attractive method because of no need for tangent linear and adjoint of the observation operator. In addition, this method can use reflectivity observations to update other thermodynamic and dynamical variables through the

^d Current affiliation: I.M. Systems Group, Inc., and NOAA/NCEP/Environmental Modeling Center, College Park, Maryland.

^e Current affiliation: NOAA/NWS/OSTI/Modeling Program Division, Silver Spring, Maryland.

Corresponding author: Dr. Chengsi Liu, cliu@ou.edu

DOI: 10.1175/MWR-D-20-0149.1

© 2021 American Meteorological Society. For information regarding reuse of this content and general copyright information, consult the AMS Copyright Policy (www.ametsoc.org/PUBSReuseLicenses).

Brought to you by UNIVERSITY OF OKLAHOMA LIBRARY | Unauthenticated | Downloaded 12/08/21 09:16 PM UTC

ensemble-based cross covariance in addition to directly related hydrometeor variables. Studies have shown positive results of using EnKF method for Z DA (e.g., Tong and Xue 2005; Jung et al. 2008; Dowell et al. 2011; Snook et al. 2012; Yussouf et al. 2013; Johnson et al. 2015). While very attractive, EnKF often suffers from insufficient ensemble spread. For example, it is possible that no ensemble member produce precipitation where precipitation is actually observed, so that Z observation is unable to correct the background error at that location. One potential solution to this is to employ a hybrid ensemble-variational (EnVar) method (Hamill and Snyder 2000) when a combination of static and ensemble background error covariances is used. To achieve this, capability to directly assimilating Z in a variational framework needs to be developed; Kong et al. (2018) compared such hybrid EnVar with EnKF for assimilate simulated radar data.

To directly assimilate Z variationally, a number of issues can arise that are related to the high nonlinearity of Z operator. Sun and Crook (1997) compared direct assimilation of Z and of rainwater retrieved from Z (under warm rain assumption) within a four-dimensional variational (4DVar) system. They found difficulties with minimization convergence because the cost function gradient of the Z observation term can be extremely large when background rainwater mixing ratio is very small, and the resulting rainwater analysis error was also larger. In their study, hydrometer (rainwater) mixing ratio was used as the control variable (CVq). As a way of overcoming the problem encountered by Sun and Crook (1997) and Carley (2012) used logarithmic mixing ratios as control variables (CVlogq) instead to assimilate reflectivity in the Gridpoint Statistical Interpolation (GSI)-based hybrid EnVar system. To avoid similar problems with large gradient of Z cost function term within an EnVar system, Wang and Wang (2017) chose to use Z as a control variable. With this approach, it is difficult to include static background error covariance term within the EnVar cost function in a traditional way for the purpose of building a hybrid EnVar system, however. Liu et al. (2020) further investigated the issues of using CVq and CVlogq when assimilating Z within a 3DVar framework and proposed several treatments to address the issues. The use of CVlogq together with several special treatments with the analysis increments is recommended in their study but all problems were not completely solved.

In addition to the logarithmic transformation, other transformations of control variables have been used in DA. Xue et al. (2010) used a power transformation for the total number concentration of hydrometeors in EnKF when assimilating Z data to reduce the dynamic range of the control variables and to better preserve sensitivity at large values. Yang et al. (2020) employed a general nonlinear power transformation within the NCEP Real Time Mesoscale Analysis system (RTMA; De Pondeca et al. 2011) to improve cloud ceiling height and surface visibility analysis. The transformed variables form a distribution that is closer to the Gaussian distribution, and reduce the errors associated with linear approximation.

The exponent of the general nonlinear power transformation employed by Yang et al. (2020) can be adjusted to control the degree of nonlinearity from purely linear (when the

exponent approaches 1) to a transformation equivalent to the natural logarithm (when the exponent approaches 0), allowing a range of possibilities and the opportunity for optimization. In this study, we implemented the nonlinear power transformation to hydrometeor mixing ratios, and use the power-transformed mixing ratios as control variables (CVpq) to assimilate Z within the GSI ensemble-3DVar (En3DVar) framework. The exponent of the power transformation affects the degree of nonlinearity in the transform and of the Z operator. The optimal value of the power transformation exponent is determined through a set of DA and forecast experiments using five severe weather cases from the 2017 NOAA Hazardous Weather Testbed Spring Forecasting Experiment (Clark et al. 2012) period. In addition, a tornado outbreak case is evaluated in more detail to further understand the differences between CVq, CVlogq, and CVpq.

The rest of this paper is organized as follows. In section 2, the GSI En3DVar algorithm, the observation operators of radar radial velocity and reflectivity, and the nonlinear power transformation are introduced. The experimental design is presented in section 3. Section 4 presents the experiment results of analyses and forecasts. Finally, a summary and conclusions are given in section 5.

2. Methodology

a. GSI En3DVar algorithm

All experiments in this study are conducted using the GSI En3DVar data assimilation system; only ensemble-based background error covariance is included, not the static background error covariance therefore the algorithm used is pure En3DVar instead of hybrid En3DVar. The implementation of the GSI hybrid En3DVar system follows the extended control variable approach of Lorenc (2003), and our brief description of the algorithm below follows Pan et al. (2014) but without the static background term in the cost function.

Within the En3DVar framework, the analysis increment $\delta\mathbf{x}$ associated with the ensemble background error covariance is defined as

$$\delta\mathbf{x} = \sum_{k=1}^K (\mathbf{x}'_k \circ \mathbf{a}_k). \quad (1)$$

In Eq. (1), K is the ensemble size, \mathbf{x}'_k is the k th ensemble perturbation normalized by $\sqrt{K-1}$, the vector \mathbf{a}_k denotes the extended control variables for the k th ensemble member. The symbol \circ denotes the Schur product or element by element product of two same-sized vectors or matrices.

The analysis increment $\delta\mathbf{x}$ can be obtained by minimizing the following cost function:

$$J(a) = \frac{1}{2} \mathbf{a}^T \mathbf{A}^{-1} \mathbf{a} + \frac{1}{2} (\mathbf{H}\delta\mathbf{x} - \delta\mathbf{y}^o)^T \mathbf{R}^{-1} (\mathbf{H}\delta\mathbf{x} - \delta\mathbf{y}^o). \quad (2)$$

Vector \mathbf{a} is formed by concatenating K vectors \mathbf{a}_k and \mathbf{A} is a block-diagonal matrix which defines the ensemble covariance localization (Lorenc 2003; Wang et al. 2007). In GSI En3DVar, the horizontal and vertical covariance localizations, or the

effects of matrix \mathbf{A} in Eq. (2), are achieved by applying recursive filter transforms (Purser et al. 2003). Also, $\delta\mathbf{y}^o = \mathbf{y}^o - H(\mathbf{x}^b)$ is the observation innovation vector, H is the observation operator and \mathbf{x}^b is the background state vector. \mathbf{H} is the tangent linear version of H and \mathbf{R} is the observation error covariance matrix. To minimize the cost function, a new variable \mathbf{z} defined as below to precondition the minimization process:

$$\mathbf{z} = \mathbf{A}^{-1}\mathbf{a}. \tag{3}$$

The cost function in (2) can be written in terms of \mathbf{z} , and avoid the appearance of \mathbf{A}^{-1} in the equation. The gradient of the cost function with respect to \mathbf{z} is given in Eq. (4), where \mathbf{D} is $[\text{diag}(\mathbf{x}'_1) \dots \text{diag}(\mathbf{x}'_k)]$:

$$\nabla_{\mathbf{z}}J = \mathbf{a} + \mathbf{A}\mathbf{D}^T\mathbf{H}^T\mathbf{R}^{-1}(\mathbf{H}\delta\mathbf{x} - \delta\mathbf{y}^o). \tag{4}$$

The final analysis can be obtained by minimizing the cost function using the conjugate gradient algorithm (Derber and Rosati 1989), utilizing the gradient calculated in Eq. (4). As in many variational data assimilation systems (e.g., Courtier et al. 1994), GSI En3DVar employs a double-loop procedure, where nonlinear observation operators are linearized within the outer loops while the cost function minimization occurs with inner-loop iterations. Within subsequent outer loops, the operator linearization occurs around an updated and improved state, hence reducing the impact of linearization approximation. Typically, only a few outer loops are needed to achieve satisfactory results.

b. Radar radial velocity and reflectivity observation operator

In this study, using GSI En3DVar, both radar radial velocity and reflectivity observations are directly assimilated. The simulated radial velocity (V_r) in GSI is calculated (Lippi et al. 2019) according to

$$V_r = u \cos\theta \cos\alpha + v \sin\theta \cos\alpha + w \sin\alpha. \tag{5}$$

In Eq. (5), u , v , and w represent zonal, meridional, and vertical velocity, respectively; θ is 90° minus the azimuth angle of the radar; and α is elevation angle of radar beams.

The reflectivity observation operator used in this study is consistent with that of Tong and Xue (2005) with default values of intercept parameters of particle size distributions set to be consistent with the one-moment Lin et al. (1983) microphysics scheme. The radar reflectivity can be defined as

$$Z = 10 \log_{10}(Z_e), \tag{6}$$

where Z_e is the equivalent radar reflectivity factor as functions of three hydrometeor mixing ratios: rainwater (q_r), snow (q_s), and hail (q_h), which can be written as follows:

$$Z_e = Z_{er}(q_r) + Z_{es}(q_s) + Z_{eh}(q_h). \tag{7}$$

In Eq. (7), Z_{er} , Z_{es} , and Z_{eh} are the equivalent radar reflectivity factors of rainwater, snow, and hail, respectively, which are defined as

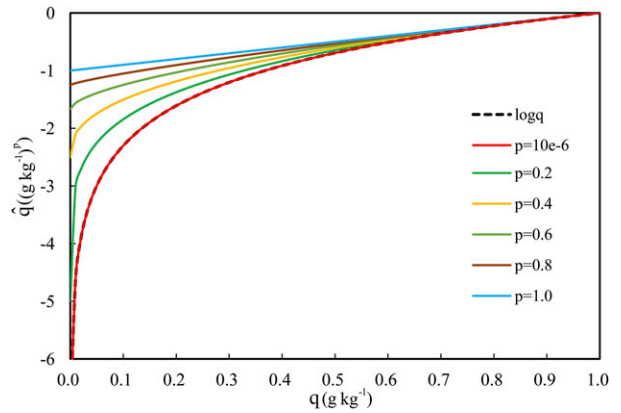


FIG. 1. The natural logarithm function and the nonlinear transformation function with different p .

$$Z_{er} = 3.63 \times 10^9 \times (\rho q_r)^{1.75}, \tag{8}$$

$$Z_{es} = \begin{cases} 9.80 \times 10^8 \times (\rho q_s)^{1.75} & T_b \leq 0^\circ\text{C}, \\ 4.26 \times 10^{11} \times (\rho q_s)^{1.75} & T_b > 0^\circ\text{C}, \end{cases} \tag{9}$$

$$Z_{eh} = 4.33 \times 10^{10} \times (\rho q_h)^{1.75}, \tag{10}$$

where ρ is the air density and T_b is the background temperature.

c. Using power transformed hydrometeor mixing ratios as control variables (CVpq)

In this study, the nonlinear transformation proposed by Yang et al. (2020) is applied to the hydrometeor mixing ratios and the transformed variables are used as the control variables in the cost function. The transformation function is defined as follows:

$$\hat{q} = \frac{(q^p - 1)}{p}, \quad 0 < p \leq 1, \tag{12}$$

where q represents the hydrometeor mixing ratio, such as q_r , q_s , or q_h ; and p is a parameter which is greater than zero and less than or equal to one. Mathematically, it is a power-law function. Figure 1 shows the natural logarithm function and the power transformation function with different p . When p approaches 0 (in this study, p is set to 1.0×10^{-6} as an approximation to 0), the nonlinear transformation function approaches natural logarithm function at the limit of 0 (i.e., $\text{CVpq} = \text{CVlogq}$). When the p value increases, the nonlinearity of Eq. (12) decreases. When $p = 1$, Eq. (12) becomes a linear function, and CVpq is equivalent to CVq . The same lower limits for hydrometeors from Liu et al. (2020) are applied on this study. Even though the smoothing function is beneficial to CVlogq when using a static background error covariance (Liu et al. 2020), we do not employ this treatment because little impact is found when using an ensemble-based background error covariance.

3. Experimental design

In this study, DA and forecast experiments are run for five different severe thunderstorm events that occurred during May 2017. The experiment domain follows the NSSL Experimental

TABLE 1. Summary of the date, the central latitude and longitude of the domain, and the severe weather report of the five cases.

Name	Date	Central latitude	Central longitude	Event description
Case1	9 May 2017	33.21°	-101.52°	Thunderstorms in eastern NM and TX Panhandle
Case2	16 May 2017	35.84°	-99.76°	Discrete tornadic thunderstorms in Elk City
Case3	18 May 2017	36.77°	-98.67°	Tornadic thunderstorms in OK and KS
Case4	23 May 2017	29.08°	-97.95°	High wind in southern TX
Case5	27 May 2017	36.77°	-93.41°	Mixed mode convection in MO, AR, and OK

Warn-on-Forecast (WoF) System (Wheatley et al. 2015). Forecasts are run at 3-km horizontal grid spacing. The domain has 250×250 grid points in the horizontal and 50 vertical levels and is centered on the severe weather event location. Experiment dates, domain locations, and a brief description of the severe weather events are provided in Table 1. Forecasts in this study are run using the WRF-ARW model version 3.8.1 and employ the following physics options: Thompson microphysics scheme (Thompson et al. 2008), the Yonsei University (YSU) planetary boundary layer scheme (Hong et al. 2006), the unified Noah land surface model (Chen and Dudhia 2001), and the Rapid Radiative Transfer Model for Global circulation models (RRTMG) shortwave and longwave schemes (Iacono et al. 2008).

The gridded Multi-Radar Multi-Sensor (MRMS; Smith et al. 2016) radar reflectivity data and the NEXRAD Level-2 radial velocity data archived at the National Climatic Data Center are used in this study. The MRMS system performs quality control and generates a mosaic of the observations on a three-dimensional grid with a horizontal resolution of 0.01° latitude \times 0.01° longitude and 33 vertical levels. A radar-preprocessing procedure of the Advanced Regional Prediction System (Brewster et al. 2005) is used to perform radial velocity data quality control and interpolate V_r data to the model grid column locations horizontally while keeping the data on radar elevation levels in the vertical for each radar site. Data thinning is not employed here. Conventional observations (e.g., surface stations, buoys, soundings) are assimilated at hourly intervals at 1800, 1900, 2000, and 2100 UTC while radar data are assimilated every 15 min throughout the 3 h. The Z and V_r observation errors are, respectively, assumed to be 5 dBZ and 1 m s^{-1} , which contain the instrument and representation error information of radar and may influence the accuracy of the analysis.

Each case study performs DA using CVpq with different parameter p values (0.0, 0.2, 0.4, 0.6, 0.8, and 1.0), where 0 and 1 correspond to CVlogq and CVq, respectively. The flowchart of the DA and forecast experiments is shown in Fig. 2. Experiments

are initialized at 1800 UTC where initial and lateral boundary conditions are provided by the High-Resolution Rapid Refresh Ensemble (HRRRE; Dowell et al. 2016). The DA window extends between 1800 and 2100 UTC; radar observations are assimilated every 15 min and conventional observations are assimilated hourly. The convergence criterion is set as 10^{-10} for the norm of the gradient. A maximum of 100 iterations is allowed for the inner-loop and 3 outer-loop iterations are used. In this study, we use a one-way coupled EnKF-En3DVar DA approach (Kong et al. 2018), in which GSI EnKF is used to update the ensemble perturbations utilized by En3DVar. The EnKF DA cycles are run independent of the En3DVar. Forecasts are initialized from the final analyses at 2100 UTC and run for 3 h until 0000 UTC.

To evaluate the impacts of using CVq, CVlogq, and CVpq on storm analyses and forecasts, the 16 May 2017 experiment is analyzed in greater depth. During this event, two cyclic supercells that are highlighted by a black square in Fig. 3a produced large hail and multiple tornadoes in eastern Texas Panhandle and western Oklahoma. The southernmost storm was initiated along a dryline boundary in Texas and became a cyclic supercell that produced an enhanced Fujita scale 2 (EF-2) tornado in Elk City, Oklahoma, around 0035 UTC. In addition to the tornado that caused extensive damage and one fatality, large hail and several additional tornado reports also produced in surrounding storms (Fig. 3b). The analyses and forecasts of storms of interest in CVq, CVlogq, and CVpq are analyzed in section 4.

4. Experimental results

The results of DA and forecast experiments using different values of parameter p with CVpq are presented in this section. The optimal p value is determined in terms of the smallest 1-h Z and V_r forecast root-mean-square innovation (RMSI), i.e., root-mean-square difference from observations. Using the optimal p value, CVpq experiments are compared with CVq and CVlogq in greater detail.

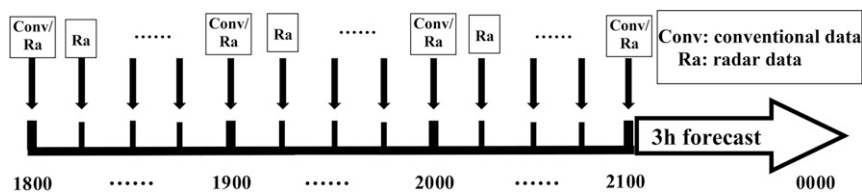


FIG. 2. The flowchart of the cycled assimilation and forecast experiments.

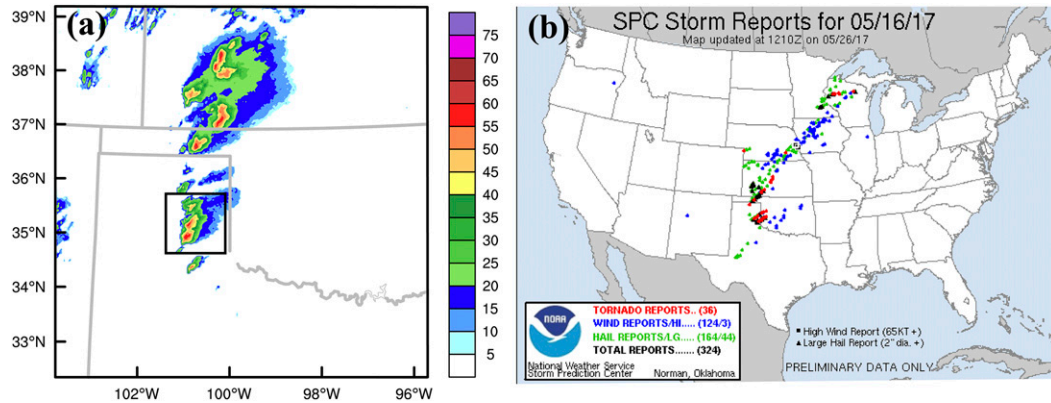


FIG. 3. (a) The composite radar reflectivity observation at 2100 UTC 16 May 2017 and (b) the storm reports of 16 May 2017 from the National Weather Service.

a. Results of experiments for optimizing parameter p

As discussed in section 2c, the degree of nonlinearity of the power transformation function depends on the value of p . To determine the optimal p value for forecast, the Z and V_r RMSIs of 60-, 120-, and 180-min forecasts using different p values of 0, 0.2, 0.4, 0.6, 0.8, or 1 for the five convective-storm cases are calculated. It is seen that Z RMSI at each forecast time is the lowest when p is 0.4 or 0.6 for all the cases (Figs. 4a1–a5) except for the 2-h forecast of 23 May case [Fig. 4a(4)], but the optimal p in terms of RMSI at different forecast time may not be the same for each case [e.g., for the 9 May case [Fig. 4a(1)], the optimal p in terms of 1- or 2-h forecast RMSI is 0.6, while that of 3-h forecast is 0.4]. The same is true for V_r RMSI (Figs. 4b1–b4) except for one when CV logq or $p = 0$ produces a smaller RMSI at each forecast time [Fig. 4b(5)]. The largest RMSI of Z is either with CV logq or CVq.

To determine an overall optimal p value in terms of lowest RMSI, the RMSIs for Z and V_r are averaged across the five cases. As shown in Fig. 5, when p is 0.4, the RMSIs of Z for all forecast time and those of V_r for 2-h forecast are the smallest; when p is 0.6, the RMSIs of V_r for 1- and 3-h forecast are the smallest.

To further quantitatively compare the Z forecast using different parameter p and determine the optimal p , the neighborhood equitable threat score (NETS; Clark et al. 2010) averaged across five cases for both low (20 dBZ) and moderately high (35 dBZ) thresholds are shown in Fig. 6. The neighborhood radius is set to 40 km, which is the same as that used in the WoF system verification for convective scale forecasts (Skinner et al. 2018). Overall, CVq (i.e., $p = 0.0$) has the lowest forecast skill for both thresholds. For the 20 dBZ threshold (Fig. 6a), CVpq0.4 (i.e., $p = 0.4$) has the best skill at the first 120 min, but then it is overtaken by CV logq (i.e., $p = 0.0$) and CVpq0.2 (i.e., $p = 0.2$). For the 35 dBZ threshold (Fig. 6b), CVpq0.4 has the best skill at the first 135 min, but then it is overtaken by CV logq and CVpq0.2. Overall, CVpq0.4 has the lowest or nearly the lowest skills for both thresholds. Because of the nonlinearity of the forecasts, the skills of shorter forecasts reflect more of the quality of the radar DA.

When forecasting thunderstorms, Z provides important storm structure information and is consequently more often evaluated than V_r . Based on the above evaluations, we regard 0.4 is the optimal parameter for p in terms of lowest RMSI. In next sections, CVpq0.4 will be compared with CVq and CV logq in further detail.

b. Results of single time analyses for the 16 May 2017 case

To see better the behaviors of DA using different control variables, we perform a single time DA analysis at 2100 UTC 16 May 2017 using CVpq0.4, CVq, and CV logq while using the background from the cycled CVq experiment. The use of the same background allows us to see more clearly the direct impact of DA.

To compare the convergence rates of the CVpq0.4, CVq, and CV logq cost functions, the cost function values and the logarithmic gradient norm with respect to inner-loop and outer-loop iterations are plotted in Fig. 7. The CVq experiment has a much slower convergence rate and does not reach the convergence criterion even at the end of the 3rd outer-loop. In addition, the logarithmic gradient norm of CVq shows numerous oscillations during the whole iterations. In contrast, the convergence rates using CV logq and CVpq0.4 are comparable during the first outer loop; the minimum cost function value is essentially reached by the 20th iteration step. CV logq satisfies the convergence criterion by the 75th iteration step while the other experiments do not by 100th iteration step. During the second and third outer loop, both CV logq and CVpq0.4 also reach the convergence criterion by around the 75th iteration step. It is suggested that CV logq has the fastest convergence rate because the logarithmic transformation results in a nearly linear relationship between Z and the control variable (logq). The relative reduction in the cost function value is somewhat larger for CVpq0.4, however.

To evaluate how the outer-loop procedures impact the Z and V_r analyses in CVq, CV logq, and CVpq0.4 experiments, the background and analysis RMSIs of Z and V_r in the three experiments at the end of the first, second, and third outer loop are compared in Fig. 8. The analysis RMSIs change relatively little when increasing the number of outer-loop for CVpq0.4

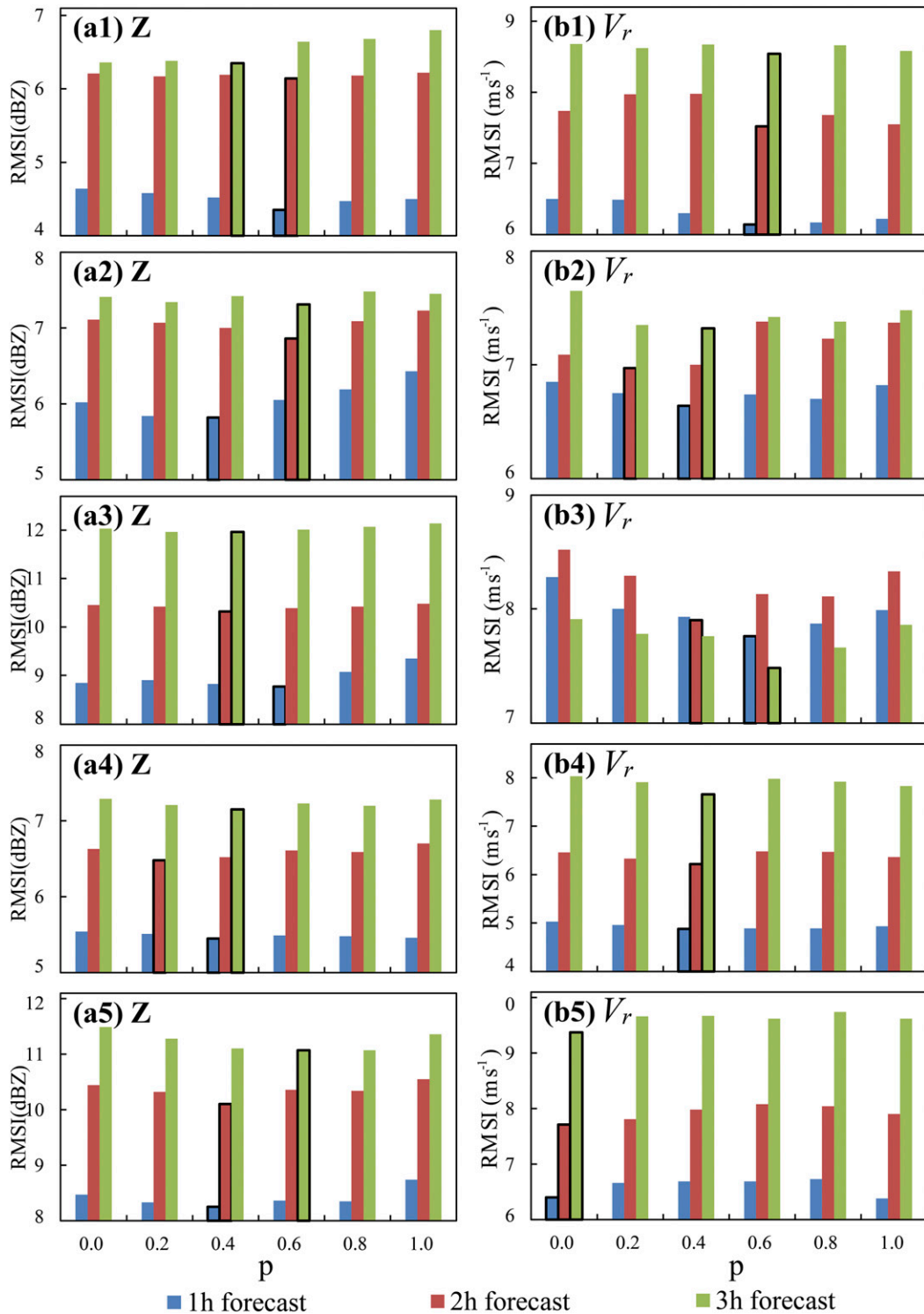


FIG. 4. (a) Radar reflectivity and (b) radial velocity RMSIs of 1-, 2-, and 3-h forecasts using different *p* values for the five cases (the five rows, see Table 1). The bar with black border represents the minimum RMSIs for each case. When *p* is 0 or 1, the results are from CV log_q and CV_q, respectively.

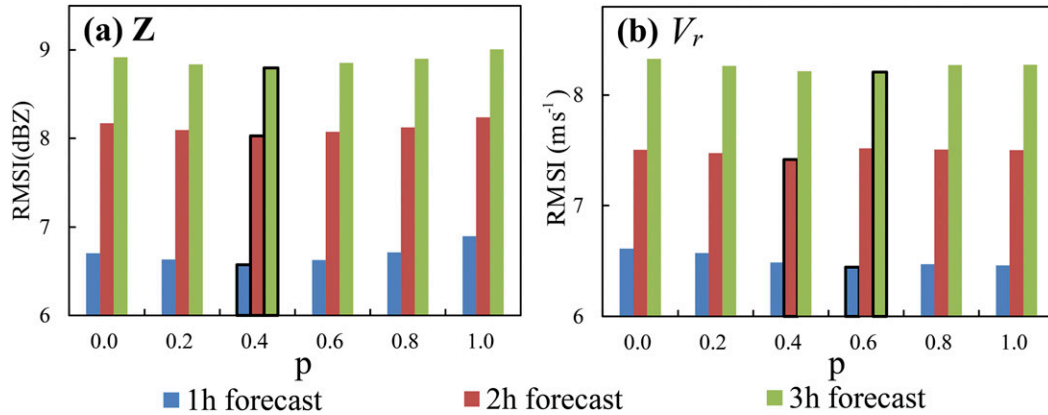


FIG. 5. As in Fig. 4, but for the averaged RMSIs of five cases.

and CV logq, which suggests the outer-loop is not very necessary in such case, presumably because the relationship between Z and control variables is more linear. For CVq, the cost function RMSI is higher than in the other two cases after one outer loop and continues to decrease in the next two outer-loops but remains higher than the other two cases. This is likely related to the higher nonlinearity of the observation operator.

It is important to note the Vr RMSI during the 1st outer-loop step for CVq is much larger than CVpq0.4 or CV logq (Fig. 8). Assimilating Vr actually becomes ineffective when Z is also assimilated at the same time when using CVq, because the gradient of cost function for the Vr term is much smaller than for the Z term (Wang and Wang 2017; Liu et al. 2020). Therefore, Liu et al. (2020) suggested the use of a separate pass to assimilate Vr within a 3DVar framework to alleviate this problem when using CVq; however, this treatment can be problematic within an En3DVar framework because cross covariances are included. When Vr data are assimilated in the second pass and the wind fields have been updated by other observations in the first pass, updated background error covariance is required. This is rarely implemented in practice because recalculating the background error covariance is

computationally expensive. Separate pass is not used in this study. With CVq, the Vr RMSI decreases as more outer-loop iterations are performed, but remains significantly larger than either CVpq0.4 or CV logq (Fig. 8).

CVq often underestimates Z in storm cores because the gradient of the cost function in these high Z regions is much smaller than in clear-air regions where the background reflectivity is much lower (Liu et al. 2020). To determine if this problem is present in our study, the Z bias (i.e., the average of observations minus the background or analysis in the observation space) in regions of high observed Z ($Z_{obs} \geq 40$ dBZ) for CV logq, CVpq0.4, and CVq is compared (Fig. 9). The forecast background (0th iteration) has large bias ($Z_{bias} > 20$ dBZ) because the predicted Z cores are much weaker than observations. After assimilating radar data, the bias substantially decreases for all experiments. CVq and CV logq have the largest and smallest Z biases, respectively (Fig. 9). The CV logq bias is relatively small (7 dBZ for all iterations) because the logarithmic transformation can effectively mitigate the bias in storm cores (Liu et al. 2020). The CVq bias decreases with more outer-loop iterations (Fig. 9), which shows the outer-loop procedure alleviates the problems associated with the nonlinear

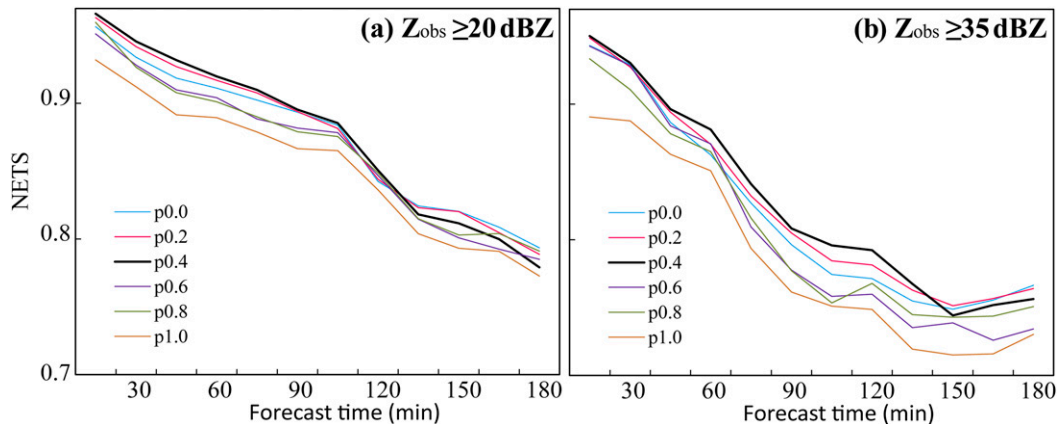


FIG. 6. The five-case average NETS of 3-h Z forecasts from the cycled analyses using different p values for (a) 20- and (b) 35-dBZ thresholds. When p is 0 or 1, the results are from CV logq and CVq, respectively.

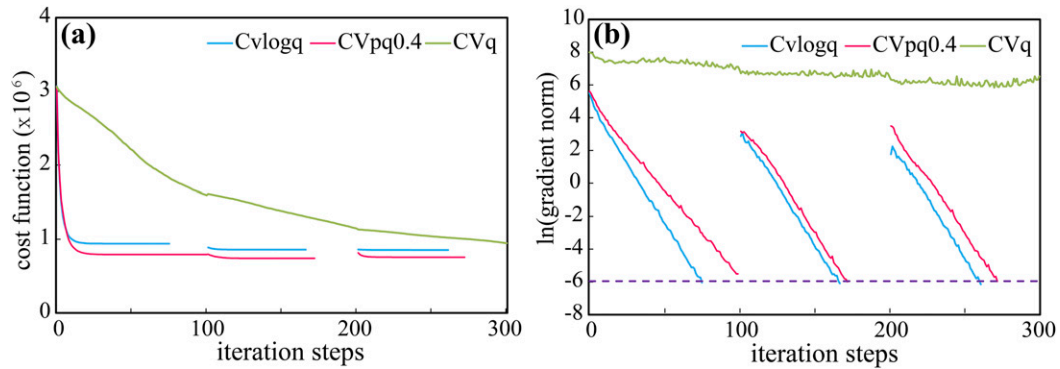


FIG. 7. (a) The cost function value and (b) logarithmic gradient norm during the inner-loop iterations of the three outer loops for CVq, CVlogq, and CVpq0.4 for the analysis of 2100 UTC 16 May 2017. The purple dashed line indicate the convergence criteria.

Z operator. As expected, the CVpq0.4 bias is between CVlogq and CVq because some nonlinearities are included in the transformation function but not as high as the logarithmic transformation.

Forecast background and the one-time analyzed Z at 2.5 km above ground level (AGL) are compared against observations in Fig. 10 within the confines of the subdomain marked in Fig. 3a. Although weaker than observed Z (Fig. 10a), the background predicts two supercells (Fig. 10b) to be in approximately the right locations as the observed ones. The background predicts the northernmost storm to exhibit a westward bias and a spurious storm in the southeastern corner of the subdomain. The CVq analysis (Fig. 10c) reduces the strength of the northern spurious storm in the background somewhat but does not suppress the spurious echoes near the southeastern corner via assimilating clear air observations due to relatively small gradient of the cost function in the background area of spurious echoes. The structures of the two main supercells are analyzed reasonably well but the intensity is obviously underestimated. The CVlogq analysis (Fig. 10d) more closely resembles observations (Fig. 10a) than CVq; it produces higher Z in the two supercells and suppresses spurious echoes found in the background (Fig. 10b) because the relatively large difference of the background gradient of the

cost function between background high- and low- reflectivity area is greatly reduced through logarithmic transform. However, CVlogq overestimates Z in the northernmost observed storm owing to the problem of logarithmic transform (Liu et al. 2020). The CVpq0.4-analyzed Z (Fig. 10e) is a blend between CVlogq and CVq, given the nonlinearity of transformation function for CVpq0.4 is between CVq (i.e., CVpq1.0) and CVlogq (i.e., CVpq0.0). It is noted that CVpq0.4 does not produce spuriously intense analysis increments in the northernmost storm but does not suppress the spurious echo in the southeast as well as CVlogq does either, suggesting that CVpq0.4 is not perfect (it does not completely eliminate nonlinearity). Compared to CVq, CVpq0.4 increases the strength of reflectivity cores and slightly reduces the strength of spurious echoes.

Vertical cross sections taken through the Z core of the supercell that produced the Elk City Tornado (dashed line in Fig. 10a) are analyzed to determine the impact of Z assimilation in CVq, CVlogq, and CVpq0.4 (Fig. 11). Prior to DA, the background Z (Fig. 11b) has smaller area coverage than observations and the analyzed echo top is 4 km lower than the observations (Fig. 11a). The CVq analysis (Fig. 11c) produces the Z associated with the anvil level reflectivity region of the storm to be above 30 dBZ. In CVlogq (Fig. 11d) and CVpq0.4 (Fig. 11e), the size of analyzed storm is larger than in CVq and

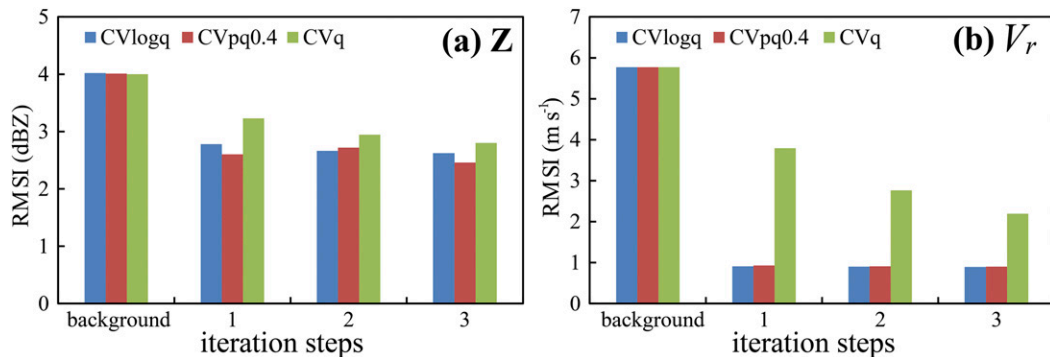


FIG. 8. The RMSIs for (a) radar reflectivity and (b) radial velocity for background forecasts and analyses using CVq, CVlogq, and CVpq0.4 at the end of each outer loop at 2100 UTC 16 May 2017.

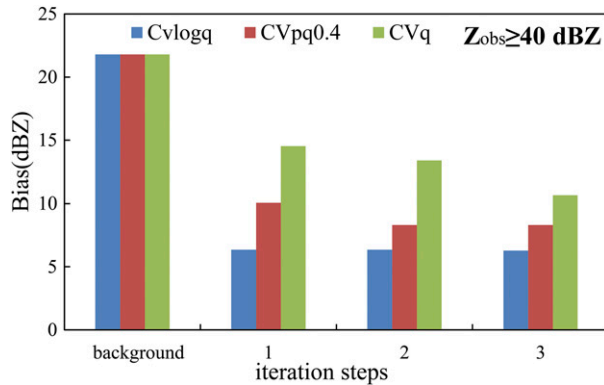


FIG. 9. Radar reflectivity bias in areas of large observed Z ($Z_{\text{obs}} \geq 40$ dBZ) of the background and the analyses of using CVq, CVlogq, and CVpq0.4 at the end of each outer loop.

more consistent with the observations while the Z cores are generally overfitted in terms of intensity. At the high levels (>10 km AGL) where radar data are sparse, CVlogq produces spuriously intense Z (Fig. 11d). The problems of overfitting observations and producing spurious Z are believed to be associated with the nonlinear nature of the transformation

(Liu et al. 2020). This problem is not observed in the CVpq0.4 analysis (Fig. 11e) because the nonlinearity is reduced.

c. Results of the 3-h forecasts initialized from 3-h cycled analyses

The 3-h forecasts of CVpq using different values of p are quantitatively evaluated in section 4a. In this section, subjective evaluations are performed to further compare CVq, CVpq0.4, and CVlogq. To compare the forecasts within 1 h when the forecast skill differences are relatively large, we plot the forecast composite Z and the observed composite Z exceeding 45 dBZ at 2200 UTC for the 16 May (Fig. 12) and 27 May (Fig. 13) cases. For the 16 May case (Fig. 12), CVlogq and CVpq0.4 predict the two supercells in the Texas Panhandle to be close to the observed storms, but CVq predicts the southernmost supercell to be displaced from observations. Although all experiments predict spurious Z echoes, CVpq0.4 does not predict any spurious echoes in the Oklahoma Panhandle. For the 27 May case (Fig. 13), The moving eastward squall line in southeastern Missouri is well predicted for all experiments but with some lag phase error. Compared to CVq and CVlogq, CVpq0.4 predicts fewer spurious storms in the eastern Oklahoma and the southern Missouri.

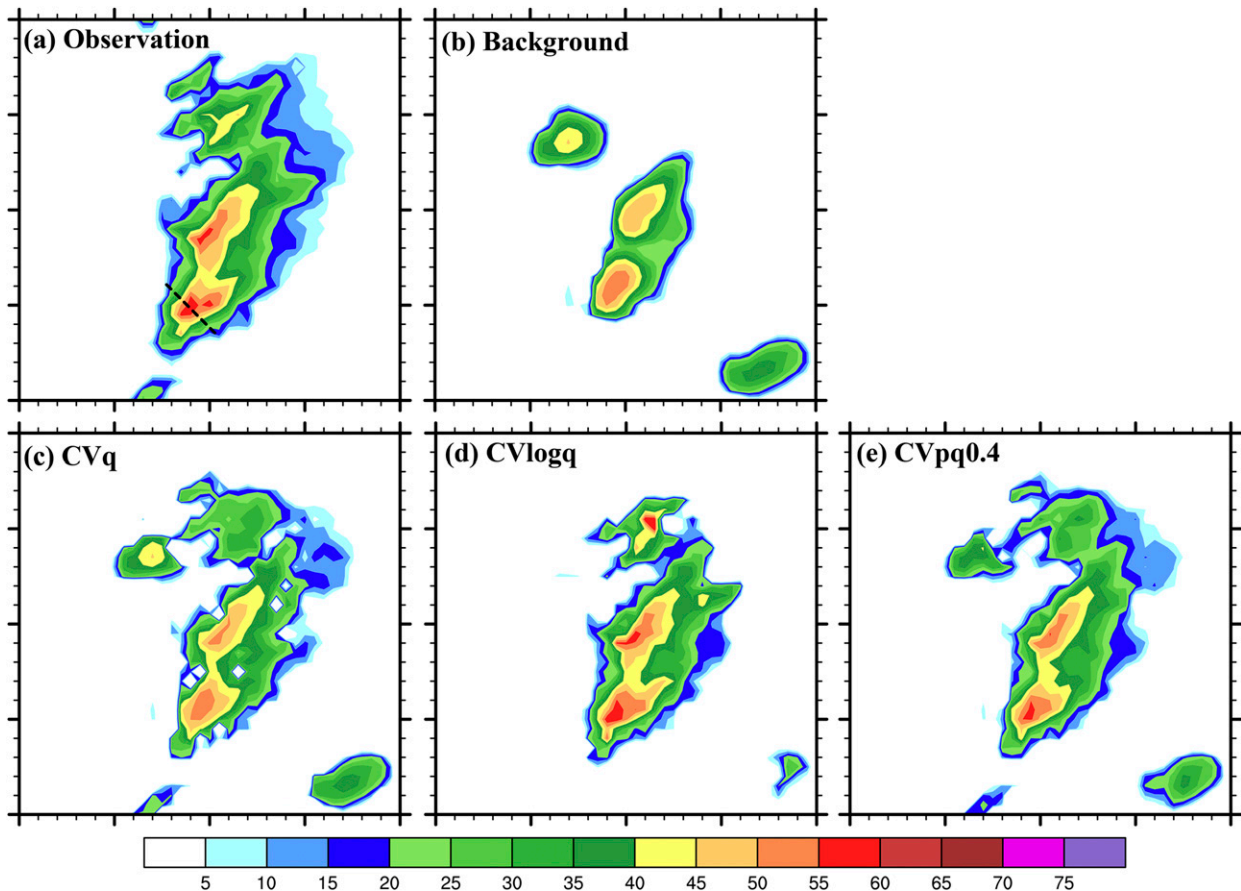


FIG. 10. The reflectivity (dBZ) at 2.5 km AGL of (a) observation, (b) background, and analyses using (c) CVq, (d) CVlogq, and (e) CVpq0.4 at 2100 UTC 16 May 2017.

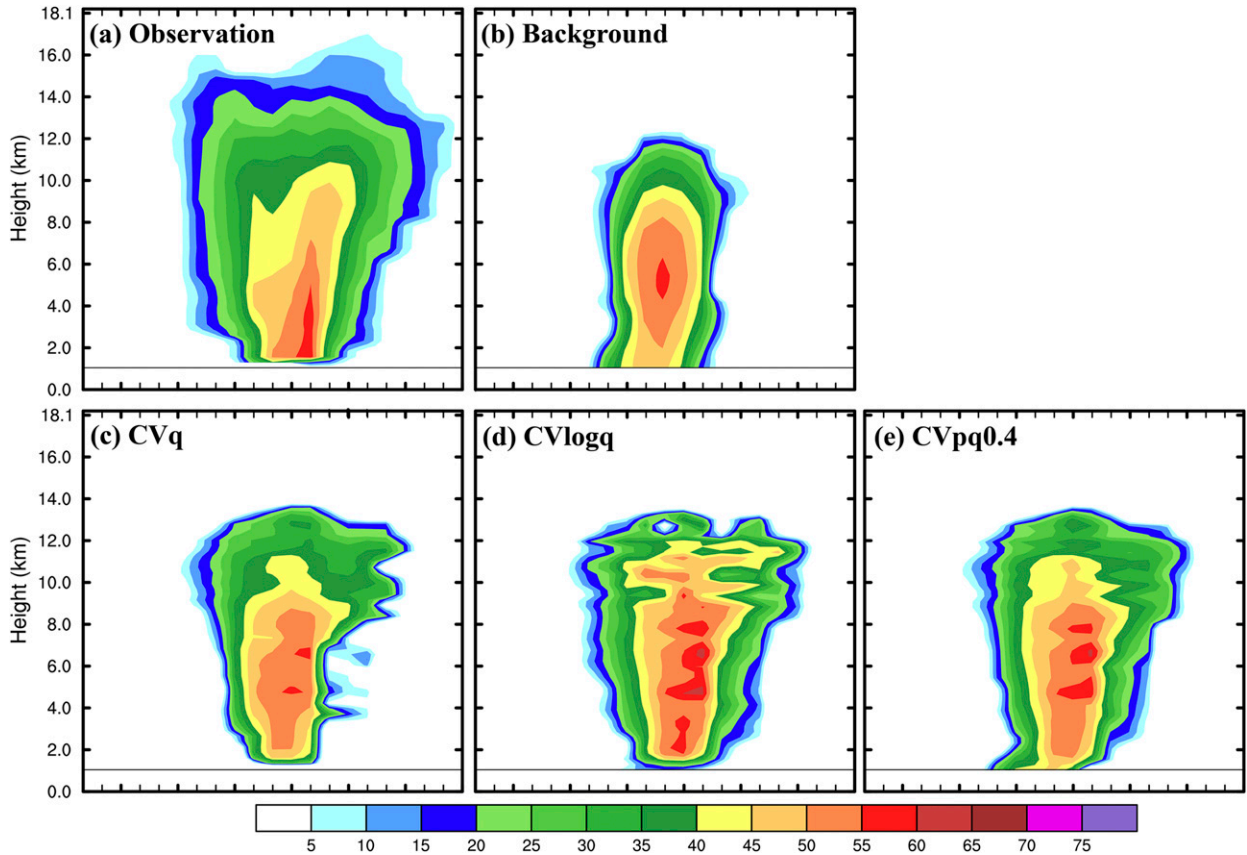


FIG. 11. As in Fig. 10, but for the reflectivity (dBZ) in vertical cross sections through the maximum reflectivity of the main storm along the dashed line in Fig. 10a.

Updraft helicity (UH) (Kain et al. 2008) is a measure of updraft rotation in the supercells and has been used as a surrogate predictor of severe weather including tornadoes with CAM forecasts (e.g., Clark et al. 2012). To examine the impacts

of different hydrometeor control variables on tornadic storm forecasts of the 16 May case, the UH in the 0–2- and 2–5-km layers AGL are calculated from model output every 5 min for the 0–3-h forecast. Rotation derived from the maximum

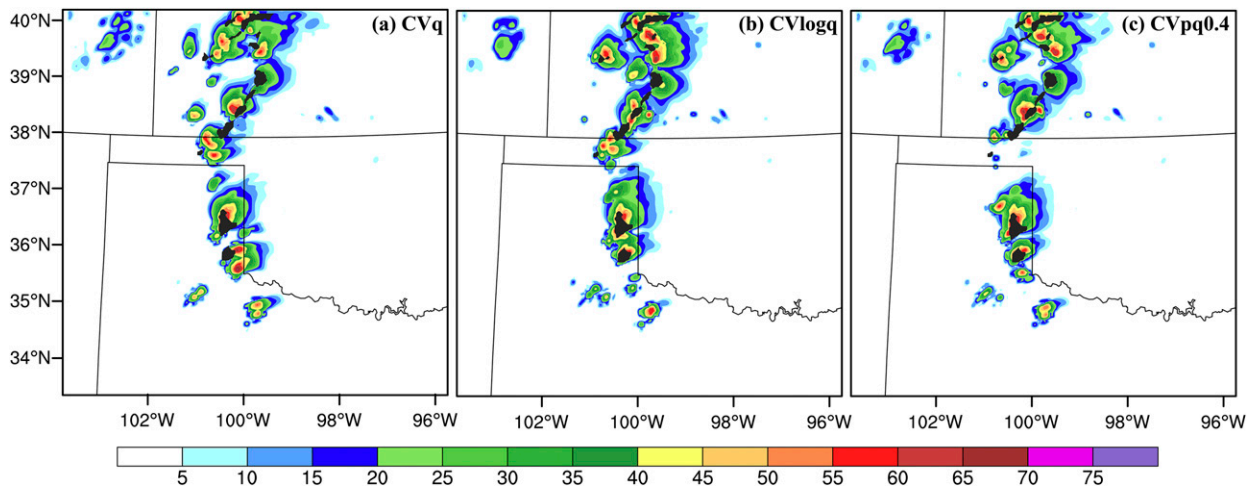


FIG. 12. The observations (black shading) over 45 dBZ and composite reflectivity (dBZ) of 60-min forecast (red shading) initialized from (a) CVq, (b) CVlogq, and (c) CVpq0.4 analyses at 2100 UTC for the 16 May case.

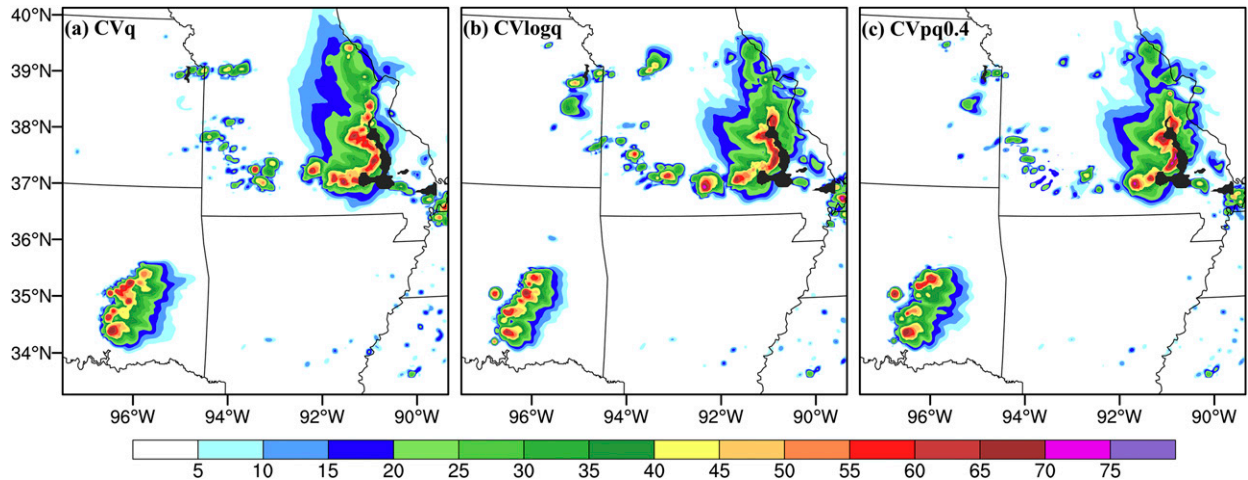


FIG. 13. The observations (black shade) over 45 dBZ and composite reflectivity (dBZ) of 60-min forecast (red shade) initialized from the (a) CVq, (b) CVlogq, and (c) CVpq0.4 analyses at 2100 UTC for the 27 May case.

range-corrected Multi-Radar Multi-Sensor (MRMS) azimuthal wind shear data (Miller et al. 2013; Newman et al. 2013) are used for 0–2- and 2–5-km UH verification. Rotation between 0 and 2 km AGL with thresholds of 0.003 83 and 0.004 13 s⁻¹, respectively, are served as observed proxies for rotation to evaluate UH

forecasts. The UH and rotation thresholds used follow Skinner et al. (2018) since the dataset and model configuration are generally similar.

CVq UH forecasts predict the southernmost supercell to be too far south and east of the observed storm [Figs. 14a(1),a(2)].

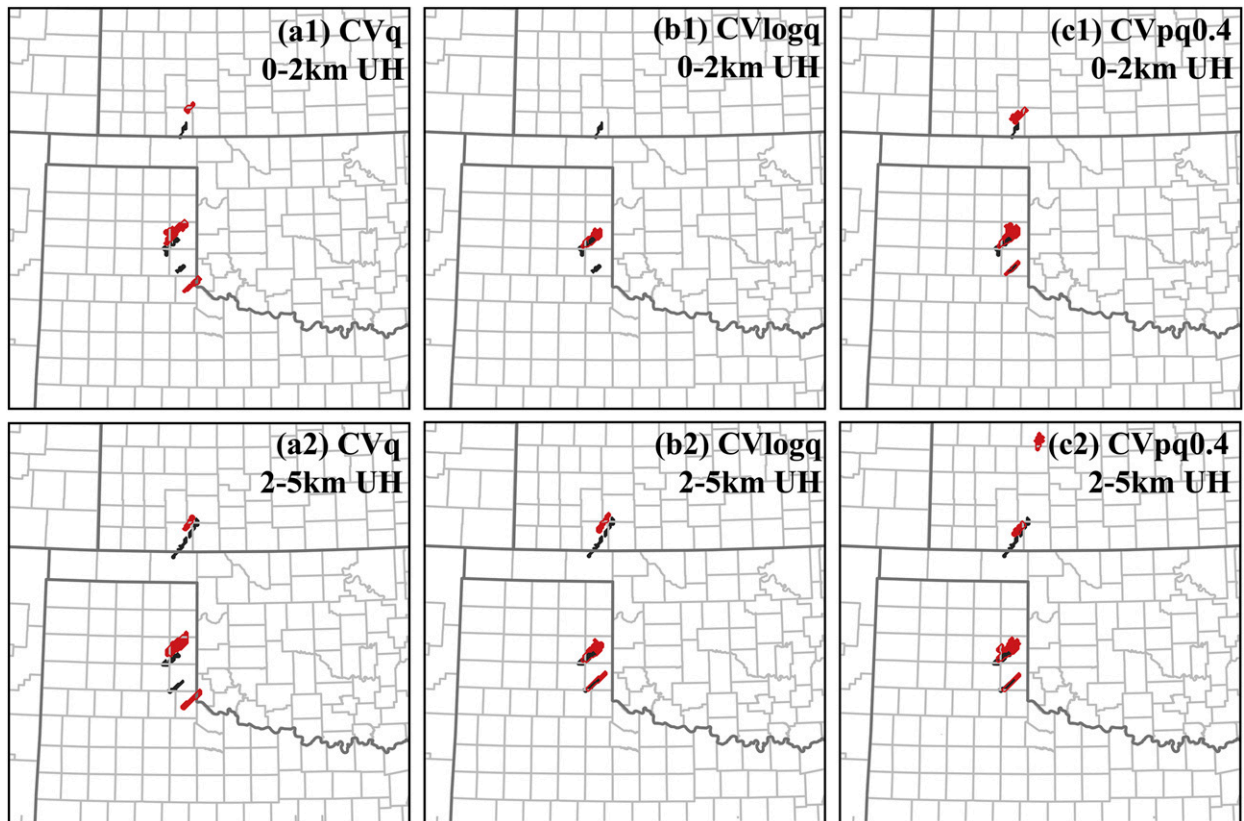


FIG. 14. The rotations derived from observations (black shading) and the forecast updraft helicity ($m^2 s^{-2}$) of 60-min forecasts valid at 2200 UTC (red shading) in the [a(1)]–[c(1)] 0–2- and [a(2)]–[c(2)] 2–5-km layers AGL.

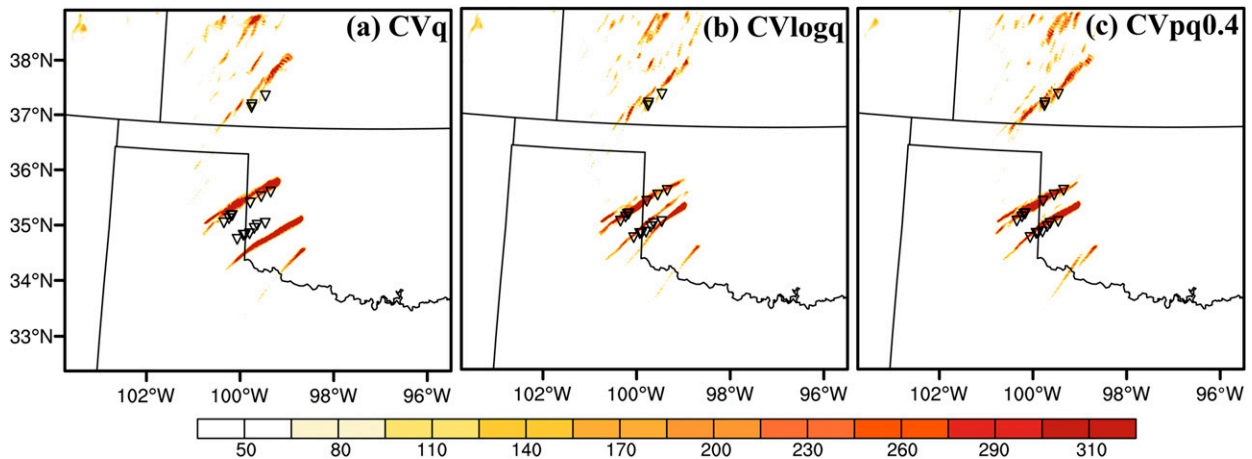


FIG. 15. The maximum 2–5-km updraft helicity track swaths ($\text{m}^2 \text{s}^{-2}$) during the 0–3-h forecasts initialized from the analyses of using (a) CVq, (b) CVlogq, and (c) CVpq0.4 at 2100 UTC 16 May 2017. The triangles represent tornado reports.

CVlogq 0–2-km UH forecast predicts the northernmost (in Northern Oklahoma) and southernmost supercells [Fig. 14b(1)] to be weaker compared to the azimuthal shear but the 2–5-km UH forecast matches the observed rotations much better [Fig. 14b(2)]. The 2–5-km UHs for the storm in southwest Kansas appear too weak for all experiments. Overall, the CVpq0.4 UH forecasts [Figs. 14c(1) and 14c(2)] exhibit more skill than CVq and CVlogq because of the smaller position and coverage mismatches between UH and observed rotations.

The maximum 2–5-km UH track swaths for 0–3-h forecast are overlaid with the Storm Prediction Center (SPC) tornado reports in Fig. 15. For CVq, a southern bias is observed in the forecast track of the southernmost supercell (Fig. 15a). This track bias is greatly reduced in CVlogq although the UH intensity is somewhat less (Fig. 15b). Also, CVlogq predicts two UH tracks instead of one for this supercell, suggesting that the structure of this supercell is not as well predicted. CVpq0.4 predicts strong and well organized UH tracks that are well collocated with the tracks of tornado reports, suggesting the most successful forecasts (Fig. 15c). In the meantime, we do realize that UH tracks are only proxies of actual tornadoes.

5. Summary and conclusions

When directly assimilating radar data within a variational framework using hydrometeor mixing ratios as control variables (CVq), the gradient of the cost function can be extremely large when the background hydrometeor mixing ratios are very small. This often prevents efficient convergence during the minimization process and can make assimilating V_r and large Z observations inefficient. These problems can be alleviated when hydrometeor mixing ratios transformed into logarithmic space are used as control variables (CVlogq) because the logarithmic transformation significantly reduces the gradient magnitude. However, when transforming the analysis increment from logarithmic space back to the original mixing ratio space, spurious analysis increments can be produced due to the high nonlinearity of this relationship.

To alleviate these problems, we apply a transform to the hydrometeor mixing ratios to form power-transformed control variables (CVpq) in this study to facilitate the direct assimilation of radar data within the GSI En3DVar DA framework. Mathematically, the proposed transform is a power-law function with a parameter p ($0 < p \leq 1$). The larger (smaller) p is, the more linear (nonlinear) the transformation function is. When $p = 1$, the nonlinear transformation function becomes a linear function (i.e., $\text{CVpq} = \text{CVq}$). When p approaches 0 (in this study, p is set to 10^{-6} as an approximation to 0), the nonlinear transformation function approaches the natural logarithm at the limit of 0 (i.e., $\text{CVpq} = \text{CVlogq}$).

The impacts of using CVq, CVlogq and CVpq on the analyses and forecasts are examined. The root-mean-square innovations (RMSIs) and neighborhood equitable threat score (NETS) for the forecasts of the five different cases using 6 different parameter values of power transform function are first evaluated to determine the optimal value, and later comparisons are focused on the use of CVq, CVlogq and CVpq0.4, with the last one being CVpq using parameter value of 0.4. The direct impacts of radar DA in the three experiments are first examined by performing a single-time analysis using the same background, and the minimization convergence rates of the cost functions are also examined. Forecasts from cycled DA using the three forms of control variables are further compared qualitatively and quantitatively. A more detailed of experiment summary and conclusions are given below.

- 1) A set of 3-h cycled DA and 3-h forecast experiments for five convective storm cases are conducted using CVpq with different parameter p (0.0, 0.2, 0.4, 0.6, 0.8, and 1.0). The optimal p value is found to be 0.4 in terms of overall lowest RMSI and highest NETS for Z forecasts, while it is found to be 0.4 or 0.6 in terms of overall lowest RMSI for V_r forecasts.
- 2) Single-time analysis experiments for the 16 May 2017 tornado storm event are run using CVq, CVlogq and CVpq0.4. The convergence rate of cost function minimization is much slower for CVq than the other experiments

because the CVq Z operator is highly nonlinear. Additionally, the adjustments to wind state variables when assimilating Z and V_r data together in CVq are very small and the analysis underestimates Z cores in the supercells. Using the outer-loop procedure for CVq can somewhat alleviate these problems but substantially increases the computational cost. For CV logq, the aforementioned problems are mostly alleviated because the relationship between Z and control variables (logq) is nearly linear. However, spurious analysis increments can occur because the logarithmic transformation is highly nonlinear. For CVpq0.4, the problems using CVq or CV logq are somewhat alleviated because some nonlinearity is included in the power transformation function but the nonlinearity is not as high as the logarithmic transformation.

- 3) The impacts of using CVq, CV logq, and CVpq0.4 on cycled DA and forecasts are further compared subjectively for the 16 May 2017 Texas and Oklahoma tornado outbreak case and the 27 May 2017 squall line case. CVpq0.4 generally outperforms CVq and CV logq for the Z and UH forecasts. In addition, for the 16 May 2017 tornado case, the UH track swaths for 0–3-h forecast are more consistent with tornado reports when using CVpq0.4.

CVpq with an optimal parameter p (0.4 in this study) exhibits the most qualitative and quantitative skill when used to directly assimilate radar data in this study. Although the CVpq is only tested in the pure En3DVar data assimilation system, it is also expected to be useful in a hybrid En3DVar data assimilation system. CVpq will be applied within a hybrid En3DVar DA framework and compared with other ensemble-based DA methods (e.g., EnKF) in future studies. The CVpq also provides a flexible framework where the p value can be further tuned.

As in many previous studies (e.g., Sun and Crook 1997; Tong and Xue 2005; Gao and Stensrud 2012), the Z observation operator used here is consistent with the one-moment Lin-type microphysics scheme. In future, we will develop and implement a Z operator consistent with the partially two-moment Thompson microphysics scheme within GSI and may apply the power transform to the total number concentrations also, in addition to hydrometeor mixing ratios.

Acknowledgments. This research was supported by the National Key R&D Program of China (2018YFC1507200), operational and technical program of Chongqing meteorological Bureau (YWJSGG-202114), NOAA Warn-on-Forecast (WoF) Grant NA16OAR4320115, and NOAA Joint Technology Transfer Initiative (JTII) Grant NA18OAR4590385. Dr. Patrick S. Skinner of NSSL is thanked for providing the code of plotting reflectivity and UH objects. Dr. Kent H. Knopfmeier of NSSL is thanked for providing the ensemble initial conditions and lateral boundary conditions data for five test cases. Dr. Runhua Yang of EMC and Jonathan Labriola of CAPS are thanked for reviewing the manuscript and discussions. Computational resources of the Oklahoma Supercomputing Center for Research and Education (OSCCER), and the NSF Xsede Supercomputing Centers were used. The severe

weather report data were downloaded from the website of the Storm Prediction Center of NOAA'S National Weather Service (<https://www.spc.noaa.gov/climo/reports>), and the NEXRAD level-2 radial velocity data were download from the website (<https://www.spc.noaa.gov/climo/reports>). Model data produced from this study have been archived at the Harvard data server (/data/chenll/CVpq/wrfout).

REFERENCES

- Albers, S. C., J. A. McGinley, D. L. Birkenheuer, and J. R. Smart, 1996: The Local Analysis and Prediction System (LAPS): Analyses of clouds, precipitation, and temperature. *Wea. Forecasting*, **11**, 273–287, [https://doi.org/10.1175/1520-0434\(1996\)011<0273:TLAAPS>2.0.CO;2](https://doi.org/10.1175/1520-0434(1996)011<0273:TLAAPS>2.0.CO;2).
- Benjamin, S. G., and Coauthors, 2016: A North American hourly assimilation and model forecast cycle: The Rapid Refresh. *Mon. Wea. Rev.*, **144**, 1669–1694, <https://doi.org/10.1175/MWR-D-15-0242.1>.
- Brewster, K., M. Hu, M. Xue, and J. Gao, 2005: Efficient assimilation of radar data at high resolution for short-range numerical weather prediction. *World Weather Research Program Symp. on Nowcasting and Very Short-Range Forecasting*, Toulouse, France, WMO, Paper 3.06.
- Carley, J. R., 2012: Hybrid ensemble-3DVar radar data assimilation for the short-term prediction of convective storms. Ph.D. dissertation, Purdue University, 205 pp.
- Chen, F., and J. Dudhia, 2001: Coupling an advanced land surface–hydrology model with the Penn State–NCAR MM5 modeling system. Part I: Model implementation and sensitivity. *Mon. Wea. Rev.*, **129**, 569–585, [https://doi.org/10.1175/1520-0493\(2001\)129<0569:CAALSH>2.0.CO;2](https://doi.org/10.1175/1520-0493(2001)129<0569:CAALSH>2.0.CO;2).
- Clark, A. J., W. A. Gallus, and M. L. Weisman, 2010: Neighborhood-based verification of precipitation forecasts from convection-allowing NCAR WRF Model simulations and the operational NAM. *Wea. Forecasting*, **25**, 1495–1509, <https://doi.org/10.1175/2010WAF2222404.1>.
- , J. S. Kain, P. T. Marsh, J. Correia, M. Xue, and F. Kong, 2012: Forecasting tornado pathlengths using a three-dimensional object identification algorithm applied to convection-allowing forecasts. *Wea. Forecasting*, **27**, 1090–1113, <https://doi.org/10.1175/WAF-D-11-00147.1>.
- Courtier, P., J. N. Thepaut, and A. Hollingsworth, 1994: A strategy for operational implementation of 4D-Var, using an incremental approach. *Quart. J. Roy. Meteor. Soc.*, **120**, 1367–1387, <https://doi.org/10.1002/qj.49712051912>.
- Derber, J., and A. Rosati, 1989: A global oceanic data assimilation system. *J. Phys. Oceanogr.*, **19**, 1333–1347, [https://doi.org/10.1175/1520-0485\(1989\)019<1333:AGODAS>2.0.CO;2](https://doi.org/10.1175/1520-0485(1989)019<1333:AGODAS>2.0.CO;2).
- De Pondeca, M. S., and Coauthors, 2011: The real-time mesoscale analysis at NOAA'S National Centers for Environmental Prediction: Current status and development. *Wea. Forecasting*, **26**, 593–612, <https://doi.org/10.1175/WAF-D-10-05037.1>.
- Dowell, D. C., L. J. Wicker, and C. Snyder, 2011: Ensemble Kalman filter assimilation of radar observations of the 8 May 2003 Oklahoma City thunderstorm: Influences of reflectivity observations on storm-scale analyses. *Mon. Wea. Rev.*, **139**, 272–294, <https://doi.org/10.1175/2010MWR3438.1>.
- , and Coauthors, 2016: Development of a High-Resolution Rapid Refresh Ensemble (HRRRE) for severe weather forecasting. *28th Conf. on Severe Local Storms*, Portland, OR, Amer. Meteor. Soc., 8B.2, <https://ams.confex.com/ams/28SLS/webprogram/Paper301555.html>.

- Duda, J. D., X. Wang, Y. Wang, and J. R. Carley, 2019: Comparing the assimilation of radar reflectivity using the direct GSI-based Ensemble-Variational (EnVar) and indirect cloud analysis methods in convection-allowing forecasts over the continental United States. *Mon. Wea. Rev.*, **147**, 1655–1678, <https://doi.org/10.1175/MWR-D-18-0171.1>.
- Evensen, G., 1994: Sequential data assimilation with a nonlinear quasi-geostrophic model using Monte Carlo methods to forecast error statistics. *J. Geophys. Res.*, **99**, 10 143–10 162, <https://doi.org/10.1029/94JC00572>.
- Gao, J., and D. J. Stensrud, 2012: Assimilation of reflectivity data in a convective-scale, cycled 3DVAR framework with hydrometeor classification. *J. Atmos. Sci.*, **69**, 1054–1065, <https://doi.org/10.1175/JAS-D-11-0162.1>.
- Hamill, T. M., and C. Snyder, 2000: A hybrid ensemble Kalman filter–3D variational analysis scheme. *Mon. Wea. Rev.*, **128**, 2905–2919, [https://doi.org/10.1175/1520-0493\(2000\)128<2905:AHEKfV>2.0.CO;2](https://doi.org/10.1175/1520-0493(2000)128<2905:AHEKfV>2.0.CO;2).
- Hong, S.-Y., Y. Noh, and J. Dudhia, 2006: A new vertical diffusion package with an explicit treatment of entrainment processes. *Mon. Wea. Rev.*, **134**, 2318–2341, <https://doi.org/10.1175/MWR3199.1>.
- Hu, M., M. Xue, and K. Brewster, 2006: 3DVAR and cloud analysis with WSR-88D level-II data for the prediction of the Fort Worth, Texas, tornadic thunderstorms. Part I: Cloud analysis and its impact. *Mon. Wea. Rev.*, **134**, 675–698, <https://doi.org/10.1175/MWR3092.1>.
- Iacono, M. J., J. S. Delamere, E. J. Mlawer, M. W. Shephard, S. A. Clough, and W. D. Collins, 2008: Radiative forcing by long-lived greenhouse gases: Calculations with the AER radiative transfer models. *J. Geophys. Res.*, **113**, D13103, <https://doi.org/10.1029/2008JD009944>.
- Johnson, A., X. Wang, J. R. Carley, L. J. Wicker, and C. Karstens, 2015: A comparison of multiscale GSI-based EnKF and 3DVar data assimilation using radar and conventional observations for midlatitude convective-scale precipitation forecasts. *Mon. Wea. Rev.*, **143**, 3087–3108, <https://doi.org/10.1175/MWR-D-14-00345.1>.
- Jung, Y., M. Xue, G. Zhang, and J. M. Straka, 2008: Assimilation of simulated polarimetric radar data for a convective storm using the ensemble Kalman filter. Part II: Impact of polarimetric data on storm analysis. *Mon. Wea. Rev.*, **136**, 2246–2260, <https://doi.org/10.1175/2007MWR2288.1>.
- Kain, J. S., and Coauthors, 2008: Some practical considerations regarding horizontal resolution in the first generation of operational convection-allowing NWP. *Wea. Forecasting*, **23**, 931–952, <https://doi.org/10.1175/WAF2007106.1>.
- Kong, R., M. Xue, and C. Liu, 2018: Development of a hybrid En3DVar data assimilation system and comparisons with 3DVar and EnKF for radar data assimilation with observing system simulation experiments. *Mon. Wea. Rev.*, **146**, 175–198, <https://doi.org/10.1175/MWR-D-17-0164.1>.
- Lin, Y.-L., R. D. Farley, and H. D. Orville, 1983: Bulk parameterization of the snow field in a cloud model. *J. Climate Appl. Meteor.*, **22**, 1065–1092, [https://doi.org/10.1175/1520-0450\(1983\)022<1065:BPOTSF>2.0.CO;2](https://doi.org/10.1175/1520-0450(1983)022<1065:BPOTSF>2.0.CO;2).
- Lippi, D. E., J. R. Carley, and D. T. Kleist, 2019: Improvements to the assimilation of Doppler radial winds for convection-permitting forecasts of a heavy rain event. *Mon. Wea. Rev.*, **147**, 3609–3632, <https://doi.org/10.1175/MWR-D-18-0411.1>.
- Liu, C., M. Xue, and R. Kong, 2020: Direct variational assimilation of radar reflectivity and radial velocity data: Issues with nonlinear reflectivity operator and solutions. *Mon. Wea. Rev.*, **148**, 1483–1502, <https://doi.org/10.1175/MWR-D-19-0149.1>.
- Lorenc, A. C., 2003: The potential of the ensemble Kalman filter for NWP—A comparison with 4D-VAR. *Quart. J. Roy. Meteor. Soc.*, **129**, 3183–3203, <https://doi.org/10.1256/qj.02.132>.
- Miller, M. L., V. Lakshmanan, and T. M. Smith, 2013: An automated method for depicting mesocyclone paths and intensities. *Wea. Forecasting*, **28**, 570–585, <https://doi.org/10.1175/WAF-D-12-00065.1>.
- Newman, J. F., V. Lakshmanan, P. L. Heinselman, M. B. Richman, and T. M. Smith, 2013: Range-correcting azimuthal shear in Doppler radar data. *Wea. Forecasting*, **28**, 194–211, <https://doi.org/10.1175/WAF-D-11-00154.1>.
- Pan, Y., K. Zhu, M. Xue, X. Wang, M. Hu, S. G. Benjamin, S. S. Weygandt, and J. S. Whitaker, 2014: A GSI-based coupled EnSRF–En3DVar hybrid data assimilation system for the operational Rapid Refresh model: Tests at a reduced resolution. *Mon. Wea. Rev.*, **142**, 3756–3780, <https://doi.org/10.1175/MWR-D-13-00242.1>.
- , M. Wang, and M. Xue, 2020: Impacts of humidity adjustment through radar data assimilation using cloud analysis on the analysis and prediction of a squall line in Southern China. *Earth Space Sci.*, **7**, e2019EA000893, <https://doi.org/10.1029/2019EA000893>.
- Purser, R. J., W. Wu, D. F. Parrish, and N. M. Roberts, 2003: Numerical aspects of the application of recursive filters to variational statistical analysis. Part I: Spatially homogeneous and isotropic Gaussian covariances. *Mon. Wea. Rev.*, **131**, 1524–1535, [https://doi.org/10.1175/1520-0493\(2003\)131<1524:NAOTAO>2.0.CO;2](https://doi.org/10.1175/1520-0493(2003)131<1524:NAOTAO>2.0.CO;2).
- Schenkman, A., M. Xue, A. Shapiro, K. Brewster, and J. Gao, 2011: The analysis and prediction of the 8–9 May 2007 Oklahoma tornadic mesoscale convective system by assimilating WSR-88D and CASA radar data using 3DVAR. *Mon. Wea. Rev.*, **139**, 224–246, <https://doi.org/10.1175/2010MWR3336.1>.
- Skinner, P. S., and Coauthors, 2018: Object-based verification of a prototype Warn-on-Forecast system. *Wea. Forecasting*, **33**, 1225–1250, <https://doi.org/10.1175/WAF-D-18-0020.1>.
- Smith, T. M., and Coauthors, 2016: Multi-Radar Multi-Sensor (MRMS) severe weather and aviation products: Initial operating capabilities. *Bull. Amer. Meteor. Soc.*, **97**, 1617–1630, <https://doi.org/10.1175/BAMS-D-14-00173.1>.
- Snook, N., M. Xue, and Y. Jung, 2012: Ensemble probabilistic forecasts of a tornadic mesoscale convective system from ensemble Kalman filter analyses using WSR-88D and CASA radar data. *Mon. Wea. Rev.*, **140**, 2126–2146, <https://doi.org/10.1175/MWR-D-11-00117.1>.
- Sun, J., and N. A. Crook, 1997: Dynamical and microphysical retrieval from Doppler radar observations using a cloud model and its adjoint. Part I: Model development and simulated data experiments. *J. Atmos. Sci.*, **54**, 1642–1661, [https://doi.org/10.1175/1520-0469\(1997\)054<1642:DAMRFD>2.0.CO;2](https://doi.org/10.1175/1520-0469(1997)054<1642:DAMRFD>2.0.CO;2).
- Thompson, G., P. R. Field, R. M. Rasmussen, and W. D. Hall, 2008: Explicit forecasts of winter precipitation using an improved bulk microphysics scheme. Part II: Implementation of a new snow parameterization. *Mon. Wea. Rev.*, **136**, 5095–5115, <https://doi.org/10.1175/2008MWR2387.1>.
- Tong, M., and M. Xue, 2005: Ensemble Kalman filter assimilation of Doppler radar data with a compressible nonhydrostatic model: OSS experiments. *Mon. Wea. Rev.*, **133**, 1789–1807, <https://doi.org/10.1175/MWR2898.1>.
- Wang, H., J. Sun, S. Fan, and X.-Y. Huang, 2013a: Indirect assimilation of radar reflectivity with WRF 3D-Var and its impact on prediction of four summertime convective events. *J. Appl. Meteor. Climatol.*, **52**, 889–902, <https://doi.org/10.1175/JAMC-D-12-0120.1>.

- , —, X. Zhang, X. Huang, and T. Auligne, 2013b: Radar data assimilation with WRF 4D-Var. Part I: System development and preliminary testing. *Mon. Wea. Rev.*, **141**, 2224–2244, <https://doi.org/10.1175/MWR-D-12-00168.1>.
- Wang, X., C. Snyder, and T. M. Hamill, 2007: On the theoretical equivalence of differently proposed ensemble/VAR hybrid analysis schemes. *Mon. Wea. Rev.*, **135**, 222–227, <https://doi.org/10.1175/MWR3282.1>.
- Wang, Y., and X. Wang, 2017: Direct assimilation of radar reflectivity without tangent linear and adjoint of the nonlinear observation operator in the GSI-based EnVar system: Methodology and experiment with the 8 May 2003 Oklahoma City tornadic supercell. *Mon. Wea. Rev.*, **145**, 1447–1471, <https://doi.org/10.1175/MWR-D-16-0231.1>.
- Wheatley, D. M., K. H. Knopfmeier, T. A. Jones, and G. J. Creager, 2015: Storm-scale data assimilation and ensemble forecasting with the NSSL Experimental Warn-on-Forecast System. Part I: Radar data experiments. *Wea. Forecasting*, **30**, 1795–1817, <https://doi.org/10.1175/WAF-D-15-0043.1>.
- Xue, M., D.-H. Wang, J.-D. Gao, K. Brewster, and K. K. Droegemeier, 2003: The Advanced Regional Prediction System (ARPS), storm-scale numerical weather prediction and data assimilation. *Meteor. Atmos. Phys.*, **82**, 139–170, <https://doi.org/10.1007/s00703-001-0595-6>.
- , Y. Jung, and G. Zhang, 2010: State estimation of convective storms with a two-moment microphysics scheme and an ensemble Kalman filter: Experiments with simulated radar data. *Quart. J. Roy. Meteor. Soc.*, **136**, 685–700, <https://doi.org/10.1002/qj.593>.
- Yang, R., R. J. Purser, J. R. Carley, M. Pondeva, Y. Zhu, and S. Levine, 2020: Application of a nonlinear transformation function to the variational analysis of visibility and ceiling height. NOAA/NCEP Office Note 502, 38 pp., <https://doi.org/10.25923/esw8-5n84>.
- Yussouf, N., E. R. Mansell, L. J. Wicker, D. M. Wheatley, and D. J. Stensrud, 2013: The ensemble Kalman filter analyses and forecasts of the 8 May 2003 Oklahoma City Tornadic thunderstorm storm using single- and double-moment microphysics schemes. *Mon. Wea. Rev.*, **141**, 3388–3412, <https://doi.org/10.1175/MWR-D-12-00237.1>.